



# Electrochemical sensor based on carbon nanotube decorated with manganese oxide nanoparticles for naphthalene determination

Ismael Carlos Braga Alves<sup>1</sup> · José Ribamar Nascimento dos Santos<sup>1</sup> · Edmar Pereira Marques<sup>1</sup> · Janyeid Karla Castro Sousa<sup>1</sup> · Maísa Azevedo Beluomini<sup>2</sup> · Nelson Ramos Stradiotto<sup>2</sup> · Aldaléa Lopes Brandes Marques<sup>1</sup>

Received: 3 March 2023 / Accepted: 21 May 2023

© The Author(s), under exclusive licence to The Japan Society for Analytical Chemistry 2023

## Abstract

In this work, an electrochemical sensor was developed for the determination of naphthalene (NaP) in well water samples, based on a glass carbon electrode (GCE) modified as a nanocomposite of manganese oxides ( $\text{MnO}_x$ ) and COOH-functionalized multi-walled carbon nanotubes (MWCNT). The synthesis of  $\text{MnO}_x$  nanoparticles was performed by the sol-gel method. The nanocomposite was obtained by mixing  $\text{MnO}_x$  and MWCNT with the aid of ultrasound, followed by stirring for 24 h. Surface modification facilitated the electron transfer process through the  $\text{MnO}_x$ /MWCNT/GCE composite, which was used as an electrochemical sensor. The sensor and its material were characterized by cyclic voltammetry (CV), transmission electron microscopy (TEM), scanning electron microscopy (SEM), energy-dispersive X-ray spectroscopy (EDS), X-ray diffraction (XRD) and Fourier transform infrared spectroscopy (FTIR). Important parameters influencing electrochemical sensor performance (pH, composite ratios) were investigated and optimized. The  $\text{MnO}_x$ /MWCNT/GCE sensor showed a wide linear range of 2.0–16.0  $\mu\text{M}$ , a detection limit of 0.5  $\mu\text{M}$  and a quantification limit of 1.8  $\mu\text{M}$ , in addition to satisfactory repeatability (RSD of 7.8%) and stability (900 s) in the determination of NaP. The determination of NaP in a sample of water from a gas station well using the proposed sensor showed results with recovery between 98.1 and 103.3%. The results obtained suggest that the  $\text{MnO}_x$ /MWCNT/GCE electrode has great potential for application in the detection of NaP in well water.

**Keywords** Naphthalene · Nanocomposite ·  $\text{MnO}_x$  · MWCNT · Electrochemical sensor

## Introduction

Polycyclic aromatic hydrocarbons (PAHs) are formed by the incomplete combustion of carbon and hydrogen-containing substances such as crude oil, coal and wood tar [1]. Some PAHs fall into a group considered for human health hazardous [2–4], because they are potentially carcinogenic compounds and can cause intoxication when ingested, inhaled or in dermal contact with very high doses [5, 6].

Consequently, PAHs are monitored worldwide in various environmental matrices [7]. They can be found in different ecosystems, such as air, soil or water, caused mainly due to industrialization, urbanization, incomplete combustion of fossil fuels (coal, diesel and oil), and other organic materials [8].

These facts have aroused the interest of researchers in developing methodologies for their determination in the environment. Thus, groundwater is considered an interesting matrix for the determination of PAHs.

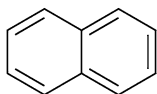
The Brazilian legislation in CONAMA resolution no. 460/2013 [9] establishes the value of 140  $\mu\text{g L}^{-1}$  in groundwater. The United States Environmental Protection Agency (EPA) has established, among the different known PAHs, 16 of them as priority hazards. NaP (molecular formula  $\text{C}_{10}\text{H}_8$ , chemical structure shown in Fig. 1) is among these 16 PAHs, since 2000, after being considered one of the great problems in an environmental and occupational sense, due to its significant carcinogenic effects [10]. NaP is a constituent of

✉ Ismael Carlos Braga Alves  
ismael.cba@ufma.br

✉ Aldaléa Lopes Brandes Marques  
aldalea.ufma@gmail.com

<sup>1</sup> NEEP (LPQA & LAPQAP), PPG-BIONORTE, Federal University of Maranhão (UFMA), São Luis, MA, Brazil

<sup>2</sup> Institute of Chemistry, São Paulo State University (UNESP), Araraquara, São Paulo, Brazil

**Fig. 1** Naphthalene molecule

diesel and jet fuel, and soil contamination from these fuels is considered a serious environmental problem [11–13].

Due to the environmental and health problems such as the caused by the NaP [5], there is a great need for the development of efficient and reliable analytical methods for their identification and quantification in groundwater [4].

EPA considers the maximum level allowed for these contaminants in drinking water to be  $0.2 \mu\text{g L}^{-1}$  [14]. On the other hand, the value considered as the maximum level of NaP by the EU in inland surface waters is  $2.0 \mu\text{g L}^{-1}$ , according to directive 2013/39/EU [15].

Chromatography, spectrometry and immunoassays are the usual methods for determining PAHs [16]. Other analytical methods have been developed for the determination of these compounds in groundwater. Electrochemical methods using different electrode materials have been applied to determine PAHs, including NaP.

Carbon is a flexible robust substrate and is widely used in the electroanalytical field as electrode material such as glassy carbon, carbon paste, carbon fiber and carbon nanotubes, increasing the charge transfer kinetics of electrodes and electrolytic interfaces [17]. Among these substrates, glassy carbon offers attractive electrochemical reactivity, negligible porosity and good mechanical stiffness, which provides a reproductive surface structure [18, 19]. Multi-wall carbon nanotubes (MWCNTs) have received increasing attention due to their high electrical conductivity, excellent mechanical strength and other extraordinary properties [20]. Furthermore, the literature reports that metal oxides combined with carbon nanotubes have superior properties when compared to their basic counterparts, thus overcoming possible electrochemical limitations due to their high electron transfer rate, long-term chemical stability, larger surface area and high robust mechanical resources [21–23].

Metal oxide nanoparticles ( $\text{MO}_x\text{NP}$ ) are dynamic materials with different applications in the scientific field. Interestingly, one-dimensional oxide provides distinctive features such as chemical and thermal stability, controlled size/morphology, low cost and fast electron communication [24]. Nanoparticles of  $\text{Fe}_3\text{O}_4$ ,  $\text{SnO}_2$ ,  $\text{TiO}_2$ ,  $\text{MnO}$ ,  $\text{ZrO}_2$ ,  $\text{WO}_3$  and  $\text{ZnO}$  have been reported as materials for determining PAHs [25, 26].

Medina-Castillo [27] developed a  $\text{Fe}_3\text{O}_4$ -MIPs sensor for pyrene determination. Li and Qu [28] studied the determination of anthracene through the structure  $\text{CA}[n]@\text{SiO}_2@\text{CdTe}$ . The author Toledo [29] determined NaP by means of the modification of  $\text{PANI}/\text{SiO}_2$  in the porous electrode. The interest in

$\text{MO}_x\text{NP}$  is justified by their non-toxicity, high stability, high electrocatalytic activity and large surface area [26, 30].

Nanocomposites based on MWCNTs- $\text{MnO}_2$  have been applied in many fields, and its application as adsorbent for PAHs has been also studied [31]. Therefore, this composite could also be combined and set as an electrochemical sensor for PAHs. In this work, a  $\text{MnO}_x/\text{MWCNT}$  nanocomposite modified glassy carbon electrode was developed as a novel electrochemical sensor for NaP.

## Experimental section

### Reagent and solutions

All chemicals used in this work were of analytical degree, and all aqueous solutions were prepared with deionized water (resistivity:  $\geq 18.2 \text{ M}\Omega \text{ cm}$ ), purified by a Milli-Q system (Millipore Inc., USA). Manganese (II) chloride tetrahydrate, acetonitrile, ethylene glycol, boric acid, sodium perchlorate monohydrate, sodium hydroxide, anthracene, benzene and dimethylformamide were obtained from Merck (Merck, Germany). NaP, toluene and xylene were obtained from the companies Supelco (Supelco, USA), Synth (Synth, Brazil) and Neon (Neon, Brazil), respectively. Multi-walled carbon nanotube functionalized with groups ( $-\text{COOH}$ ) was supplied by DropSend (DropSend, S.L, Spain). Sulfuric acid, acetic acid, phosphoric acid and nafion® were purchased from Sigma-Aldrich (Sigma-Aldrich, USA). A Britton-Robinson (BR) buffer solution was prepared by mixing solutions of phosphoric acid, acetic acid, boric acid and sodium perchlorate at a concentration of 0.1 M. The pH was adjusted by the addition of sodium hydroxide solution (2.0 M). The NaP stock solution was prepared in 1:1 (v/v) water/acetonitrile.

### Equipment and materials

The infrared spectra (FTIR) of the synthesized materials ( $\text{MnO}_x/\text{MWCNT}$ ) were recorded by the Shimadzu IR Prestige-21 spectrometer in the region of the wavelength range from  $400$  to  $4000 \text{ cm}^{-1}$ , deactivated and prepared on KBr pellets (1.0%). X-ray diffraction (XRD) analyses were performed using a Bruker D8 Advance diffractometer using  $\text{Cu K}\alpha$  radiation in the  $2\theta$  angle range ( $10^\circ$ – $80^\circ$ ). The mean size ( $d$ ) of the nanoparticles was evaluated by applying the Scherrer equation below [32]:

$$d = \frac{0.94\lambda}{\beta \cos \theta} \quad (1)$$

where “ $\lambda$ ” is the wavelength of the X-rays (0.154 nm), “ $\beta$ ” is the width at half the height of the analyzed peak, and  $\theta$  is the Bragg angle.

Transmission electron microscopy (TEM) images were recorded using a Philips CM200. Scanning electron microscopy (SEM) and energy-dispersive X-ray spectroscopy (EDS) were performed on a Hitachi TM 3030 instrument.

The electrochemical experiments were performed at atmospheric pressure and room temperature in a conventional three-electrode cell using a potentiostat model PGSTAT 302 from Metrohm Autolab connected to a computer with the NOVA 2.1 software. A GCE (geometric area = 0.07 cm<sup>2</sup>), Ag|AgCl|KCl<sub>sat</sub> and platinum wire were used as the working, reference and auxiliary electrodes, respectively.

### MnO<sub>x</sub> nanoparticles synthesis and preparation of the MnO<sub>x</sub>/MWCNT nanocomposite

The synthesis of MnO<sub>x</sub> nanoparticles was performed by the sol-gel method. 3 g of MnCl<sub>2</sub>·4H<sub>2</sub>O was dissolved in ethylene glycol (50 mL) into the solution at 50 °C, and the solution was heated until reach 80 °C to form the gel, after this solution was then stirred at room temperature for 2 h and dried in an oven at 150 °C. Then, it was ground in a mortar and placed in a muffle furnace at 600 °C for 3 h (heating rate of 5 °C min<sup>-1</sup>) [33]. The MnO<sub>x</sub>/MWCNT nanocomposite was prepared according to the procedure reported in the literature [34]. First, the manganese oxide was dispersed in dimethylformamide and sonicated for 30 min. Afterward, MWCNT was added and more 30 min of sonication was performed. Then, the resulting suspension was placed under agitation for 24 h. After this period, the material was centrifuged for 30 min at 2400 rpm. The supernatant was discarded, and the precipitate was washed with distilled water successive times to remove possible impurities and oven-dried at 50 °C for 1 h.

### Electrode preparation

Initially, the GCE was polished using an alumina suspension (0.05 μm) on a felt, and electrochemically polished by successive scans in a potential range between 1.0 and -1.5 V in 0.5 M H<sub>2</sub>SO<sub>4</sub>, at 50 mV s<sup>-1</sup>, until obtaining the cyclic voltammogram with characteristics of a clean GCE. The modified GCE was prepared using a suspension containing 5.0 mg mL<sup>-1</sup> of nanocomposite (MnO<sub>x</sub> nanoparticles and MWCNT) in deionized water with 0.5% nafion®. The mixture was homogenized in an ultrasonic bath for 30 min at room temperature. Subsequently, a 10 μL aliquot of the resulting suspension was dripped onto the GCE surface, which was then dried at room temperature to allow the solvent to evaporate and obtain the MnO<sub>x</sub>/MWCNT/GCE.

To characterize the properties of the MnO<sub>x</sub>/MWCNT/GCE, voltammograms were registered in BR buffer pH 1.8, using the scan rate (*v*) of 50 mV s<sup>-1</sup> in the 0.0–1.6 V

potential range. The optimization of the composite of MnO<sub>x</sub> and MWCNT was performed in different proportions (1:1, 2:1, 3:1 and 1:2 m/m) in order to ensure high selectivity, robustness, and allow to determine low concentrations of NaP.

### Electrochemically active surface area

The electrochemically active surface area (ECSA) can be estimated through the electrical double-layer capacitance (*C*<sub>DL</sub>) and the specific capacitance (*C*<sub>s</sub>) according to Eq. 2. This approach is often used to determine the surface area of different materials [35]. *C*<sub>DL</sub> measurements occurred at different scan rates, in a small potential range, where no occur faradaic processes [36].

$$ECSA = \frac{C_{DL}}{C_s} \quad (2)$$

*C*<sub>s</sub> is defined as the specific capacitance of the sample or the capacitance of an ideal flat surface of the material. The actors Barton and Infield [37] describe procedures to find standardized values of *C*<sub>s</sub> in acidic or basic media. However, measuring *C*<sub>s</sub> values is not practical for different systems. McCrory [38] reported different *C*<sub>s</sub> values taking into account different materials in acidic solutions, typical values range reported for *C*<sub>s</sub>, from 0.015 to 0.11 mF cm<sup>-2</sup> in H<sub>2</sub>SO<sub>4</sub> and from 0.022 to 0.130 mF cm<sup>-2</sup> in NaOH and KOH solutions. According to these studies, *C*<sub>s</sub> values may vary for different materials [38, 39]. In this work, the value of *C*<sub>s</sub> = 0.035 mF cm<sup>-2</sup> was adopted according to the literature [36, 38].

The *C*<sub>DL</sub> was determined in an H<sub>2</sub>SO<sub>4</sub> 1.0 M solution, measuring the non-faradaic capacitive current associated with a given potential at different scan rates (from 10 to 80 mV s<sup>-1</sup>) in the range of 0.65–0.75 V vs. Ag/AgCl [36].

### Real sample preparation

The groundwater sample was collected from a well of a gas station located in the city of São Luís, Maranhão State, Brazil. The sample was collected in an amber glass bottle previously cleaned with Extran® solution and oven-dried at 100 °C for 24 h. During the collection, the amber glass bottle containing the sample was kept in an ice bath and then taken to the laboratory and stored at a controlled temperature (~4.0 °C) for a maximum period of 20 days. The sample was diluted with BR buffer solution, pH 1.8, in the proportion of 1:1 (v/v) in order to perform the electrochemical measurements by differential pulse voltammetry (DPV). The concentrations of NaP in the sample were determined by the standard addition method. In order to carry out the recovery analysis, known amounts of NaP were added to the original

sample, using the methodology proposed by Burns, Danzer, and Townshend [40].

## Analytical procedure

Ten mL of 0.1 M BR solution (pH 1.8) containing NaP from standard solution (analytical curve) or from the sample was added to the electrochemical cell. Electrochemical measurements performed by CV were recorded in the potential range of 0.0–1.6 V at a scan rate of 0.05 V s<sup>-1</sup>. All solutions analyzed by DPV were realized using the parameters indicated in item “[Optimization of DPV parameters for NaP analysis.](#)”

## Results and discussion

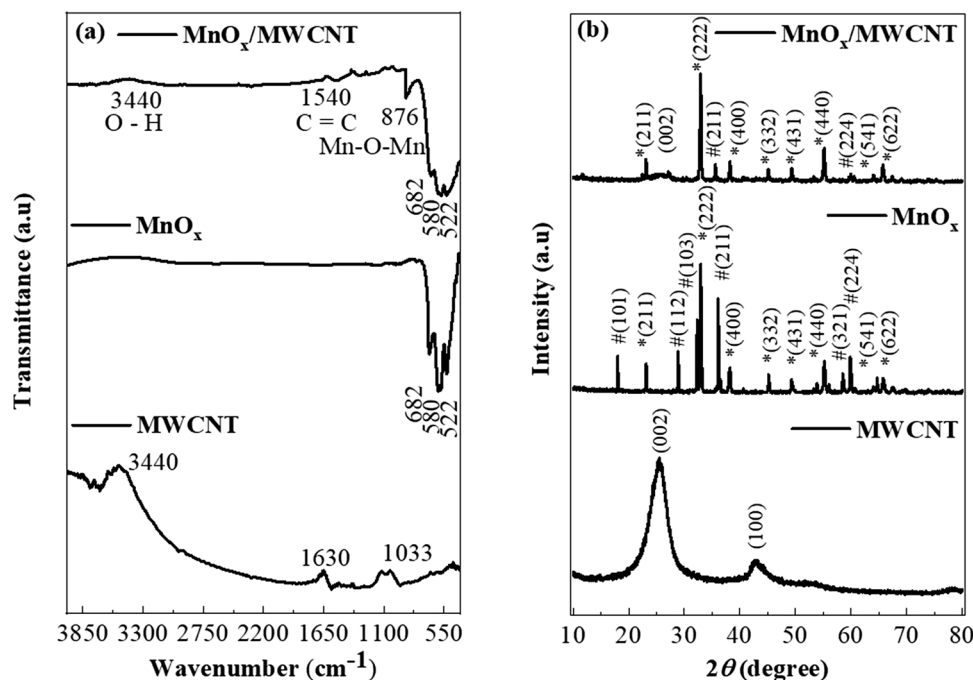
### Physical–chemical characterization

The FTIR spectra in the region from 400 cm<sup>-1</sup> to 4000 cm<sup>-1</sup>, obtained for MnO<sub>x</sub>, MWCNT and MnO<sub>x</sub>/MWCNT, are shown in Fig. 2a. For the MWCNT functionalized with COOH- groups, the bands at 3440 cm<sup>-1</sup>, 1630 cm<sup>-1</sup> and 1033 cm<sup>-1</sup> are assigned to the stretching vibrations of (O–H), (C=O) and (C–O), respectively [34, 41]. The spectra obtained for MnO<sub>x</sub> provided intense bands at 522, 580 and 682 cm<sup>-1</sup> generated as Mn–O stretching vibrations [42]. The formation of the nanocomposite MnO<sub>x</sub>/MWCNT was verified due to the presence of all characteristic bands of MnO<sub>x</sub> and MWCNT in the spectrum of the nanocomposite MnO<sub>x</sub>/MWCNT, confirming the incorporation of the nanoparticles.

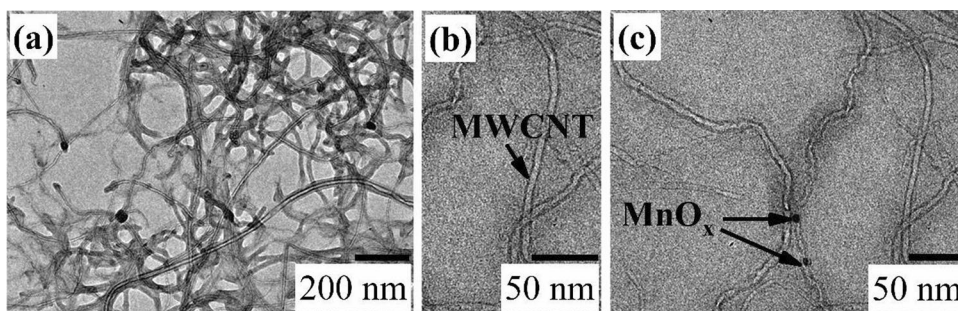
The crystal structures were evaluated by XRD (Fig. 2b). Peaks indexed for MWCNT at 2θ of 25.6° and 42.1° correspond to the (002) and (100) reflection planes, characteristic of carbon [34, 43]. The peaks in the diffractogram obtained for MnO<sub>x</sub> were indexed as a spinel structure (JCPDS no. 041-1442). In this case characteristic peaks of Mn<sub>2</sub>O<sub>3</sub> (highlighted with \* symbol) are displayed at 2θ values of 23.1°, 32.9°, 38.2°, 45.1°, 49.3°, 55.2°, 64.2°, 65.8° and 67.5° corresponding to the (211), (222), (400), (332), (431), (440), (541), (622) and (631) planes, respectively [34, 44]. Furthermore, diffraction peaks at 2θ of 18.0°, 28.9°, 32.4°, 36.2°, 58.6° and 59.9° (highlighted with # symbol) are assigned to Mn<sub>3</sub>O<sub>4</sub> (JCPDS no. 24-0734), corresponding to its (101), (112), (103), (211), (321) and (224) facets, respectively [44]. The diffraction pattern of MnO<sub>x</sub>/MWCNT presents peaks characteristic of MWCNT in addition to peaks similar to those observed for MnO<sub>x</sub>, confirming the presence of MWCNT and MnO<sub>x</sub> in the composite. The average crystal size was calculated using Eq. 1 [32] for the highest intensity peaks from the diffractograms in Fig. 2b. The average crystal size of the nanoparticles was 3.3 and 39.9 nm for MWCNT and MnO<sub>x</sub>, respectively. For the composite MnO<sub>x</sub>/MWCNT, the average size found was 29.6 nm. These results indicate the efficiency of the method used to obtain nanoparticles. The elemental analysis of the MnO<sub>x</sub>, MWCNT and MnO<sub>x</sub>/MWCNT nanomaterials was performed by the EDS technique, and the morphology was evaluated using the TEM and SEM technique. Figure 3 shows the TEM images of the MnO<sub>x</sub>/MWCNT nanocomposite and MWCNT.

Figure 3a presents an overview of the nanocomposite at the 200 nm scale. As can be observed the uniform

**Fig. 2** **a** FTIR spectra of MnO<sub>x</sub>, MWCNT and MnO<sub>x</sub>/MWCNT samples. **b** X-ray diffractograms of MnO<sub>x</sub>, MWCNT and MnO<sub>x</sub>/MWCNT



**Fig. 3** TEM of **a** MnO<sub>x</sub>/MWCNT (200 nm) **b** MWCNT (50 nm) and **c** MnO<sub>x</sub>/MWCNT (50 nm) nanocomposite



distribution of MnO<sub>x</sub> nanoparticles in the MWCNT, form a porous network structure, able to accommodate volume changes, as well as offering many reactive sites, facilitating rapid electron transport. Figure 3b shows the structure of the MWCNT more clearly with a scale of 50 nm. Furthermore, Fig. 3c indicates the presence of manganese oxide in MWCNTs, confirming the obtaining of the nanocomposite (MnO<sub>x</sub>/MWCNT).

In Fig. S1a it is possible to clearly visualize the morphology of MnO<sub>x</sub> nanoparticles, showing that the MnO<sub>x</sub> has irregularity in relation to the sizes of MnO<sub>x</sub> clusters. In Fig. S1b, it is possible to observe the insertion of MnO<sub>x</sub> on the surface of the carbon nanotube, maintaining its morphological characteristics. The EDS (Fig. S1c) confirms the presence of manganese and oxygen atoms in the composition of MnO<sub>x</sub>, with a small amount of carbon due to calcination residue. The EDS of MnO<sub>x</sub>/MWCNT composite (Fig. S1d) confirms the presence of MnO<sub>x</sub> regarding the presence of carbon, showing that the composite was successfully obtained.

### Electrochemical characterization of MnO<sub>x</sub>/MWCNT/GCE

To determine the *EC*SA of MnO<sub>x</sub>/MWCNT/GCE, voltammograms were recorded as described in the “[Electrochemically active surface area](#)” section. The results are shown in

Fig. 4a for the MnO<sub>x</sub>/MWCNT/GCE. The linear increase in current density with scan rate increase clearly indicates the charging and discharging of the Helmholtz double layer [35].

The double-layer charging current is equal to the product of the scan rate,  $\nu$ , by the double-layer electrochemical capacitance  $C_{DL}$ , and can be determined by Eq. 3 [38].

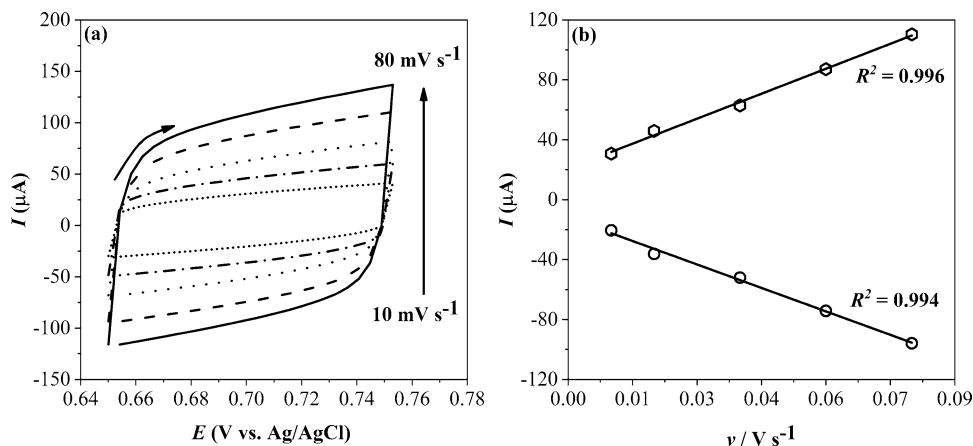
$$I_c = \nu \times C_{DL} \quad (3)$$

where  $I_c$  is the current obtained at a given potential and  $\nu$  is the scan rate. Thus, a plot of  $I_c$  versus  $\nu$  produces a straight line with slope equal to  $C_{DL}$  (Fig. 4b), on which the current was plotted vs.  $\nu$  considering  $E = 0.75$  V. The slopes  $I_a = 1.1$  mF and  $I_c = -1.0$  mF were obtained. The average value of the slopes modules (1.1 mF) represents the value of  $C_{DL}$  (Eq. 3). With this value in hand, it was possible to calculate the *EC*SA value through Eq. 2, that is 30.7 cm<sup>2</sup>, a value close to those obtained in the literature [45].

To study the electrochemical characteristics of the modified GCE, CV technique was used. Figure 5a shows the voltammetric responses of GCE (curve a), MnO<sub>x</sub>/GCE (curve b), MWCNT/GCE (curve c), and MnO<sub>x</sub>/MWCNT/GCE (curve d), in BR buffer pH 1.8, using a scan rate of 50 mV s<sup>-1</sup>, recorded in the 0.0–1.6 V potential range.

For data interpretation, the Pourbaix diagram for manganese was used [46]. As expected, no oxidation or reduction peaks were observed in the voltammograms for the GCE

**Fig. 4** **a** CVs curves of MnO<sub>x</sub>/MWCNT/GCE at different scan rates between 10 and 80 mV vs. Ag/AgCl in 1.0 M H<sub>2</sub>SO<sub>4</sub>; **b** the corresponding cathodic and anodic charging current densities measured at 0.75 V vs. Ag/AgCl plotted as a function of scan rate



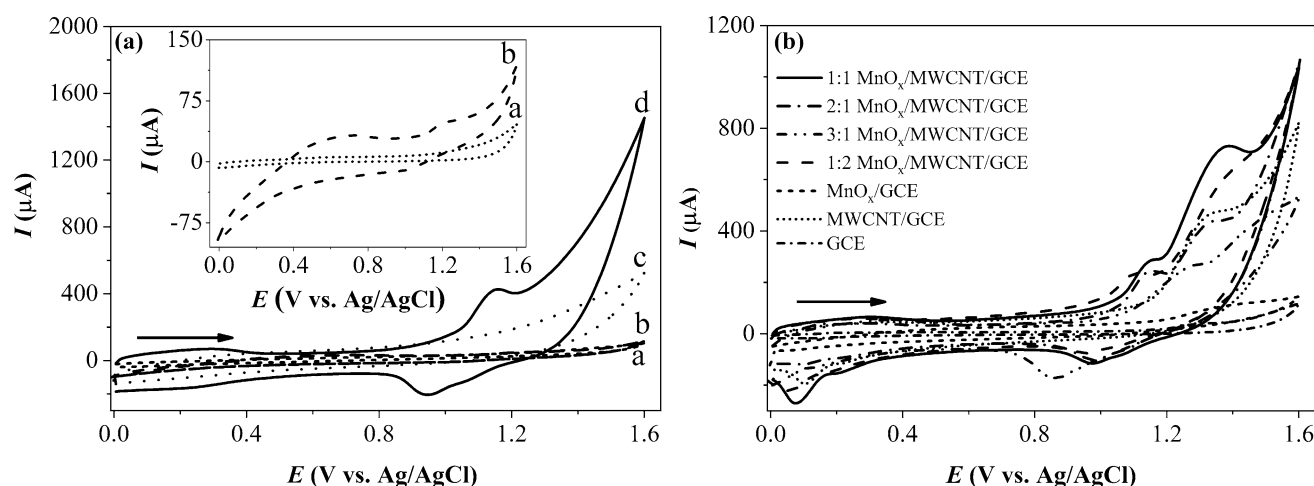


**Fig. 5** **a** CVs of GCE (curve a),  $\text{MnO}_x/\text{GCE}$  (curve b), MWCNT/GCE (curve c) and 1:1  $\text{MnO}_x/\text{MWCNT}/\text{GCE}$  (curve d) in BR buffer pH 1.8, scan rate was of  $50 \text{ mV s}^{-1}$ . Inset shows curves a and b in

magnification for better viewing. **b** CVs obtained for the different electrodes in BR buffer (pH = 1.8) and presence of 1.0 mM NaP at a scan rate of  $50 \text{ mV s}^{-1}$ .

(curve a) and MWCNT/GCE (curve c) in the aforementioned supporting electrolyte. However, for the  $\text{MnO}_x/\text{GCE}$  and  $\text{MnO}_x/\text{MWCNT}/\text{GCE}$ , different voltammetric peaks are observed, attributed to redox processes that occur during the electrochemical formation of manganese oxides ( $\text{Mn}_3\text{O}_4$ ,  $\text{Mn}_2\text{O}_3$  and  $\text{MnO}_2$ ). The potential range between 0.3 and 0.6 V is associated with the formation of  $\text{Mn}_2\text{O}_3$  [47]. The change in the voltammetric profile of the electrode containing MWCNT is probably due to the electrocatalytic response of the MWCNT on the surface of the GCE, besides improving the current conductivity and increasing the active surface area. The anodic peak near 1.2 V is formed by the oxidation of  $\text{Mn}_2\text{O}_3$  to produce  $\text{MnO}_2$ , in accordance with the Pourbaix diagram for manganese in acidic medium [46]. The corresponding cathodic peak close to 0.95 V refers to the reduction of the  $\text{Mn}^{4+}$  present in  $\text{MnO}_2$ , leaving the elevated oxidation state to the  $\text{Mn}^{2+}$  state [48–50].

The mass ratio of the  $\text{MnO}_x/\text{MWCNT}$  composite (1:1, 2:1, 3:1 and 1:2 m/m) exerts a direct influence on the film thickness, and its effect on the voltammetric behavior was evaluated in BR buffer, pH 1.8 (Fig. S2). The evaluation of the best conditions was analyzed in terms of anodic peak current ( $I_{\text{ap}}$ ) and potential ( $E_{\text{ap}}$ ) obtained for each composition studied. For the 1:1, 2:1, 3:1 and 1:2 mass ratios, the  $I_p$  values were 0.43 mA, 0.28 mA, 0.30 mA and 0.32 mA, respectively. The  $E_p$  values found were 1.15 V, 1.15 V, 1.31 V and 1.11 V, respectively. Therefore, it was possible to infer that the mass ratio with the best voltammetric performance was 1:1  $\text{MnO}_x/\text{MWCNT}$ , revealing that  $\text{MnO}_x$  increases the reaction sites and the surface area in relation to the modified electrode only with MWCNT or  $\text{MnO}_x$ . These results show that the synergistic effect of the materials improved the electrochemical activity of the electrode.

It is also possible to notice an increase in double-layer capacitance current for the 1:1  $\text{MnO}_x/\text{MWCNT}$  ratio, which indicates that the material was deposited on the electrode surface, forming an electronically conducting film [51]. Furthermore, a shift in potential is observed for the mass ratio of 3:1, possibly due to excess  $\text{MnO}_x$  on the surface of the GCE.

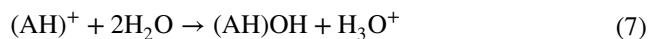
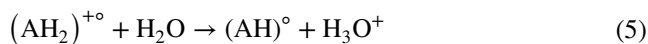
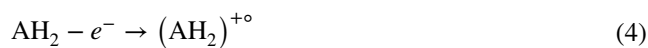
The electrochemical behavior of NaP using GCE, MWCNT/GCE,  $\text{MnO}_x/\text{GCE}$  and  $\text{MnO}_x/\text{MWCNT}/\text{GCE}$  was evaluated by the CV technique in BR buffer (pH = 1.8) containing 1.0 mM NaP (Fig. 5b). For the  $\text{MnO}_x/\text{MWCNT}$  nanocomposite, different compositions were evaluated (1:1, 2:1, 3:1 and 1:2 m/m).

Considering that the oxidation potential for the  $\text{MnO}_x/\text{MWCNT}$  is at 1.15 V, it is possible to notice a second anodic peak at 1.30 V, referring to the oxidation of NaP.

All electrodes tested showed an anodic peak attributed to NaP oxidation; however, the 1:1  $\text{MnO}_x/\text{MWCNT}/\text{GCE}$  exhibited the best response with a current of  $732.0 \mu\text{A}$  and a peak potential of 1.30 V associated with NaP oxidation in the 1:1  $\text{MnO}_x/\text{MWCNT}/\text{GCE}$  molar ratio, which is 1.7 times higher when compared to the MWCNT/GCE ( $430.0 \mu\text{A}$ ), 22.1 times higher when compared to the GCE ( $33.1 \mu\text{A}$ ) and 6.4 times higher when compared to the  $\text{MnO}_x/\text{GCE}$  ( $114 \mu\text{A}$ ). In the case of ratios of 2:1 and 3:1 for  $\text{MnO}_x/\text{MWCNT}/\text{GCE}$ , the observed decrease in the oxidation current of NaP when compared to the ratio 1:1 of  $\text{MnO}_x/\text{MWCNT}/\text{GCE}$  is probably due to excess  $\text{MnO}_x$  on the surface of the electrodes, which impaired the transfer of electrons from the analyte to the transducer. For the ratio of 1:2  $\text{MnO}_x/\text{MWCNT}/\text{GCE}$ , the decrease in the peak current may be associated with the inhibition of  $\text{MnO}_x$  nanoparticles, caused by the increase in the amount of MWCNT in the nanocomposite. For the ratio of 3:1 of

MnO<sub>x</sub>/MWCNT/GCE, in addition to a decrease in current, a peak shift to higher potentials (1.5 V) was also observed. For the different electrodes tested, the cathodic peak observed around 0.08 V is related to the by-products of NaP oxidation [52]. According to the literature [53], the oxidation of NaP on the MnO<sub>x</sub>/MWCNT/GCE can occur through the production of radical cations, which are hydrated, leading to the formation of by-products, the most stable of which being the species 1,4-naphthoquinones and binaphthyl [53, 54].

The common mechanism of electrochemical transmission in arenes indicates a radical cation formation (Eq. 4), where AH<sub>2</sub> is the aromatic hydrocarbon and (AH<sub>2</sub>)<sup>•+</sup> is the radical cation. After the formation of the cation, they can trigger different secondary reactions. One of the most important reactions is the abstraction of the hydronium ion to form the neutral radical (Eq. 5). The radical produced can be re-oxidized (Eq. 6) to form the carbocation, which subsequently reacts with the nucleophile to obtain the hydroxylated compound (Eq. 7). The resulting hydroxylated product can be re-oxidized again to form more stable compounds such as the major product, 1,4-naphthoquinones [53–55].



### Electrochemical behavior and feasibility for NaP electroanalysis

The effect of scan rate on the electrochemical behavior of NaP in MnO<sub>x</sub>/MWCNT/GCE was analyzed by CV using 1.0 mM NaP in BR buffer, pH 1.8. The CVs were obtained at different scan rates ranging from 10 to 100 mV s<sup>-1</sup> (Fig. 6a). The linear relationship between *I*<sub>p</sub> vs. *ν* (Fig. 6b) indicates that the reaction of the analyte on the electrode surface modified with MnO<sub>x</sub>/MWCNT/GCE is controlled by an adsorptive process. The log *I*<sub>p</sub> vs. log *ν* plot (Fig. 6c) shows a good linear relationship with a slope of 0.8. This value is

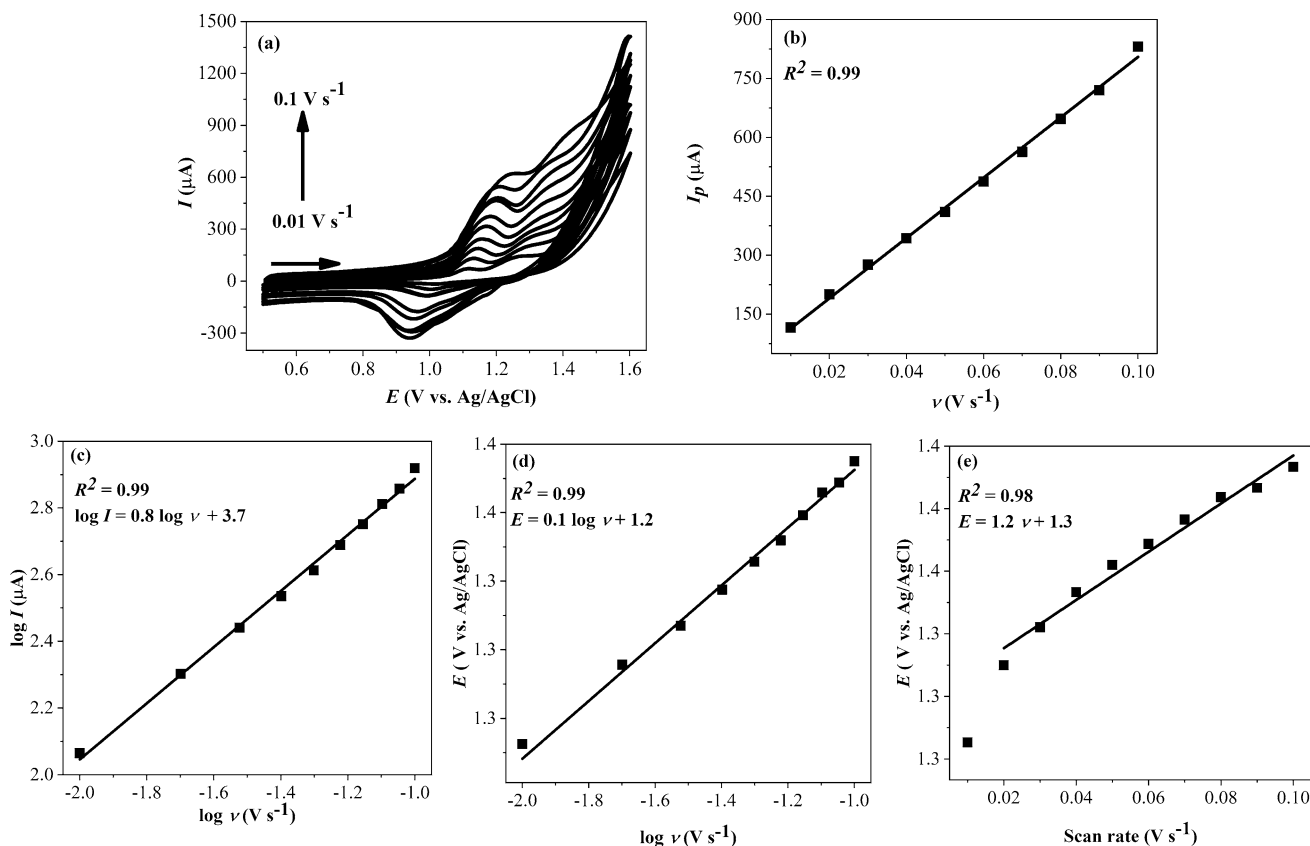


**Fig. 6** a CVs of MnO<sub>x</sub>/MWCNT/GCE in the presence of NaP (1 mM), in BR buffer pH (1.8) with different scan rate (10 mV s<sup>-1</sup>–100 mV s<sup>-1</sup>). b Ratio of *I*<sub>p</sub> vs. *ν*; c log *I*<sub>p</sub> vs. log *ν*; d *E* vs. log *ν* and e *E* vs. *ν*

close to the theoretical value of 1.0 [56], which is typical of adsorption-driven redox processes. This result is in agreement with previous studies for the determination of NaP [3].

Figure 6d shows the relationship of  $E$  vs.  $\log v$ , and is expressed by the Laviron equation (Eq. 8) [57].

$$E = E^0 + 2.303RT/\alpha nF [\log (RTK_0/\alpha nF) - \log v] \quad (8)$$

where ' $\alpha$ ' is the charge transfer coefficient for the molecule oxidation, ' $k_0$ ' is the standard rate constant of the surface reaction, ' $v$ ' is the scan rate ( $\text{V s}^{-1}$ ), ' $E^0$ ' is the formal redox potential (V), ' $T$ ' is the temperature (K), ' $R$ ' is the universal gas constant ( $8.314 \text{ J K}^{-1} \text{ mol}^{-1}$ ), ' $n$ ' is the number of electrons involved in the rate-determining step, and ' $F$ ' is Faraday's constant ( $96,485 \text{ C mol}^{-1}$ ). According to experiments performed, the relationship between the oxidation peak potentials of NaP and  $\log v$  ( $0.01\text{--}0.1 \text{ V s}^{-1}$ ) is given by equation  $E = 0.1 \log v + 1.2$  (Fig. 6d). Thereby, one can calculate ' $\alpha n$ ' according to the slope of the equation. The value found was 0.4, and as reported by Bard and Faulkner [58], the theoretical value of  $\alpha$  for an irreversible process is 0.5, so the value for ' $n$ ' is approximately 1. The result found for ' $n$ ' indicates that one electron has been involved in the oxidation of NaP.

The  $k_0$  value was also calculated to inform about the speed of the electron transfer process of NaP oxidation on the electrode surface. For this, Eq. 8 was used. The value of  $E^0$  was obtained using the graph  $E^0$  vs.  $v$  (Fig. 6e), in which the intercept of the linear regression equation is the value of  $E^0$ , in this case 1.3 V vs. Ag/AgCl. Hence, it was possible to obtain  $k_0$  in the value of  $24.5 \text{ s}^{-1}$  at 298 K. The surface concentration of NaP at  $\text{MnO}_x/\text{MWCNT}/\text{GCE}$  was calculated using the following equation [59].

$$I_p = n^2 F^2 A \Gamma v / 4RT \quad (9)$$

In Eq. 9, ' $A$ ' is the active surface area of the sensor in  $\text{cm}^2$ , ' $v$ ' is scan rate, ' $n$ ' is the number of electrons, ' $I_p$ ' is the respective peak current, and ' $\Gamma$ ' is the surface concentration in  $\text{mol cm}^{-2}$ . The  $\Gamma$  of NaP for bare GCE and  $\text{MnO}_x/\text{MWCNT}/\text{GCE}$  was found to be  $1.4 \times 10^{-8} \text{ mol cm}^{-2}$  and  $2.2 \times 10^{-7} \text{ mol cm}^{-2}$ , respectively.

The pH is one of the main factors affecting the performance of electrochemical sensors. Due to this, the effect of pH on the oxidation of 1.0 mM NaP in  $\text{MnO}_x/\text{MWCNT}/\text{GCE}$  was studied by the CV technique using BR buffer in the pH range of 1.0–6.0. The study in pH 1.0 was carried out using  $\text{H}_3\text{PO}_4$  0.1 M. Figure S3 shows  $I_p$  vs. pH plot ( $E_p = 1.4 \text{ V}$ ), where pH 1.8 was the most suitable to be used in the analysis of NaP in  $\text{MnO}_x/\text{MWCNT}/\text{GCE}$ . As this pH yielded the highest current intensity, with good peak definition for NaP oxidation, so it was selected for the subsequent experiments.

The interference of the  $\text{MnO}_x/\text{MWCNT}/\text{GCE}$  sensor was evaluated in the presence of the following possible

foreign compounds in water: ions (sodium, potassium and calcium), benzene, toluene, xylene, anthracene and pyrene. Using the concentration of NaP as being  $6.0 \mu\text{M}$ , in BR buffer (pH 1.8), the ratios of 1:1 and 1:10 (analyte: possible interferent) were evaluated, respectively. The results obtained in the presence of these compounds showed relative standard deviation values ranging from  $-2.4\%$  to  $3.1\%$ , as can be observed in Table S1. Based on these results, one can conclude that the proposed method using DPV did not present significant interference for NaP detection in the presence of these possible interferents.

### Optimization of DPV parameters for NaP analysis

To determine NaP by DPV using  $\text{MnO}_x/\text{MWCNT}/\text{GCE}$ , firstly the basic parameters of this technique (pulse amplitude, scan rate and pulse time) were optimized. All these measurements were realized in buffer BR (pH = 1.8) in the presence of NaP ( $50 \mu\text{M}$ ). Pulse amplitude was tested in the range of 10–100 mV scan rate in the range of 10–100  $\text{mV s}^{-1}$ , pulse time was optimized in the range of 100 ms to 250 ms. Based on these experiments (data not shown), the following parameters were chosen and used for all further measurements: amplitude = 90 mV, scan rate =  $60 \text{ mV s}^{-1}$  and pulse time = 100 ms. The optimal voltametric parameters were chosen not only due to the highest  $I_p$  but also considering the resolution (good definition) of the NaP peak wave.

### Analytical curve for NaP

After optimization of the parameters, the calibration curves were constructed using the  $\text{MnO}_x/\text{MWCNT}/\text{GCE}$  sensor. DPV has been selected for NaP analysis, using  $\text{MnO}_x/\text{MWCNT}/\text{GCE}$ , since it is one of the most sensitive voltammetric techniques.

Figure 7 shows the voltammograms and corresponding analytical curve for NaP. The increase in the NaP oxidation peak at 1.3 V, due to the increase in its concentration in the medium, results in a decrease in the peak close to 1.08 V, which is attributed to the  $\text{Mn}^{3+}/\text{Mn}^{4+}$  redox pair (Fig. 7a). This indicates clearly that there is an interaction between the analyte and the composite as result of the redox process.

The constructed analytical curve shows good linearity in the concentration range between  $2.0 \mu\text{M}$  and  $16 \mu\text{M}$  of NaP, as shown in Fig. 7b. The linear regression presented an  $R^2$  of 0.99, where  $I_p = 1.1 \text{ NaP } (\mu\text{M}) - 1.8 \times 10^{-6}$  is the mathematical equation that defines the analytical curve for NaP.

The values referring to standard deviation (SD) and the slope of the calibration curve ( $S$ ) were used to determine limit of detection (LOD) and limit of quantification (LOQ), through the classical statistical approach based on the IUPAC definitions and ACS [60] that shows that

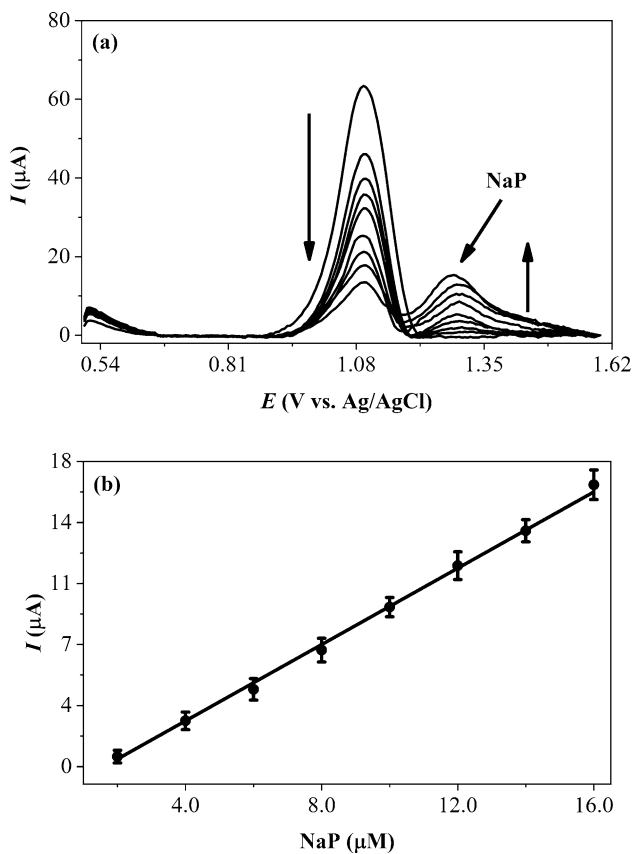


**Fig. 7** **a** DPVs of the  $\text{MnO}_x/\text{MWCNT}/\text{GCE}$  electrode for NaP at different concentrations (2.0  $\mu\text{M}$  to 16  $\mu\text{M}$ ) as a function of the concentration in BR buffer pH 1.8. Parameters: scan rate ( $\nu$ )=60  $\text{mV s}^{-1}$ , pulse amplitude 90 mV. **b** Analytical curve NaP concentration ( $\mu\text{M}$ ) vs.  $I_p$

these limits =  $k \times (\text{SD}/S)$  with factor  $k = 3$  and 10, respectively. The relative standard deviation (RSD) values obtained for the slope and the intercept were 3.6% and

2.9%, respectively. LOD and LOQ values were 0.5  $\mu\text{M}$  and 1.8  $\mu\text{M}$ , respectively, for  $n = 3$ .

### Comparison of the proposed electrochemical sensor with others in the literature

Table 1 shows a comparison of the sensor of the present study with sensors reported in the literature for the determination of NaP in different matrices. The  $\text{MnO}_x/\text{MWCNT}/\text{GCE}$  has a sensitivity close to that obtained by other authors. It is worth mentioning that depending on the structure of the material, the electrode may present a more sensitive response, especially when the miniaturization of the system under study occurs, for example, works involving microelectrodes printed, the literature reports good performance with low detection limits [3, 61]. Among the works presented, the  $\text{MnO}_x/\text{MWCNT}$  electrode presents practicality in the preparation of the modification, compared to other works reported, which require greater complexity in the methodology, requiring a longer preparation time, which increases the cost of obtaining the material, and of the electrochemical sensor. Thus, the sensor  $\text{MnO}_x/\text{MWCNT}$  has a low LOD, despite not being the most sensitive, when compared to others in the literature. It is important to note that the GCE modified with the  $\text{MnO}_x/\text{MWCNT}$  composite provided a simple electrochemical sensor for NaP determination. In addition, no studies were found in the literature using this electrode.

Although some have greater sensitivity, the sensor proposed in this work is comparable to at least two of the works in Table 1 and has some advantages and peculiarities (simplicity and preparation time), which may justify its importance and application.

**Table 1** Comparison of different electrochemical sensors for the determination of NaP

Electrode	Method	Linear range, NaP ( $\mu\text{mol L}^{-1}$ )	LOD, NaP ( $\mu\text{mol L}^{-1}$ )	References
Mn/MWCNT/GCE	DPV	2.0–16.0	0.5	This work
PBCSO <sub>3</sub> Na/Graphene/GCE <sup>a</sup>	DPV	0.01–0.1	$1.4 \times 10^{-3}$	[2]
PANI/SiO <sub>2</sub> /MPS <sup>b</sup>	IES	0.2–7.4	0.2	[29]
Ti <sub>3</sub> C <sub>2</sub> -mXene/BP/LIPG <sup>c</sup>	LSV	0.02–40.0	$1.6 \times 10^{-3}$	[62]
E-rGO/SPE <sup>d</sup>	DPV	0.05–1.2	$1.5 \times 10^{-2}$	[3]
Thiolated Calix[4]arene/CdSe/QDs/HMDE <sup>e</sup>	SWV	1.5–25.0	0.8	[63]

<sup>a</sup>Water-soluble conjugated polyelectrolyte controlled self-assembly with graphene by the LBL assembly technique (PBCSO<sub>3</sub>Na/Graphene/GCE)

<sup>b</sup>Polyaniline oxide growth macroporous silicon layer passivated (PANI/SiO<sub>2</sub>/MPS)

<sup>c</sup>Phosphorene nanohybrid with graphene-like titanium carbide mXene on the flexible substrate surface of laser-induced porous graphene (Ti<sub>3</sub>C<sub>2</sub>-mXene/BP/LIPG)

<sup>d</sup>Electrochemical reduction of graphene oxide screen-printed electrode (E-rGO/SPE)

<sup>e</sup>Thiolated Calix [4] arene, cadmium selenide quantum dots hanging mercury drop electrode (Thiolated Calix [4] arene/CdSe/QDs/HMDE)

## Repeatability and stability of MnO<sub>x</sub>/MWCNT/GCE

The electrode repeatability was evaluated by six successive NaP measurements (6.0 μM) using the DPV technique, with MnO<sub>x</sub>/MWCNT/GCE. Through the average value of peak currents (2.5 μA), it was possible to calculate the RSD (7.8%), which indicates that the electrode has good precision. The performance of MnO<sub>x</sub>/MWCNT/GCE was also evaluated in terms of stability using the chronoamperometry technique in the presence of NaP at a concentration of 1.0 mM. The study was carried out with a constant potential of 1.3 V for a period of 1000 s. As shown in Fig. S4, the process reaches stability after a few seconds (~ 100 s) maintaining the current around 0.09 mA throughout the remaining time (900 s), which confirms its stability. In addition, the MnO<sub>x</sub>/MWCNT/GCE was storage at room temperature (25 °C) for 20 days and after this period the electrode still showed approximately 90% of the initial current, proving to have good stability.

## Application of the method in real sample

To verify the performance and applicability of the procedure, the electrochemical sensor was applied in the determination of NaP concentration in well water samples from a gas station, using the standard addition method. DPV signals were recorded (data not shown) under optimized conditions as described in Fig. 7. Table 2 presents a summary of the analytical parameters referring to the determination of NaP in a real sample. Based on the linear regression obtained, it was possible to determine the NaP concentration as being ~ 8.75 ± 1.6 μM, considering the dilution process described in the section “Real sample preparation”.

The results referring to the recovery study are summarized in Table 3. The results show a variation from 98.1 to 103.3%, which indicates that the method has a relatively good degree of accuracy, and the proposed sensor can be successfully applied in the determination of NaP in well water samples.

**Table 2** Analytical parameters in the determination of NaP in real samples—Conditions as Fig. 7

Parameter	NaP
Linear range	2.0–12 μM
Linear equation	$I_p = 0.64 \text{ NaP} (\mu\text{M}) + 2.8 \times 10^{-6}$
Correlation coefficient	0.998

**Table 3** Determination of NaP levels in groundwater samples ( $n=3$ ) by the DPV method

Sample	Add (μM)	Found (μM)	Recovery (%)	RSD (%)
Gas station well water	–	2.9 ± 0.1	–	–
	2.0	4.9 ± 0.1	101.6	2.2
	4.0	6.8 ± 0.2	98.1	2.9
	6.0	9.0 ± 0.3	101.8	2.1
	8.0	11.1 ± 0.4	102.5	1.1
	10.0	13.3 ± 0.3	103.3	4.1
	12.0	14.7 ± 0.2	98.3	1.1

## Conclusion

In this work, an electrochemical sensor based on GCE modified with the nanocomposite MnO<sub>x</sub>/MWCNT was developed for the detection of NaP. The combination of MWCNT with the MnO<sub>x</sub> nanoparticles was of fundamental importance in the obtained performance for the electrode, presenting good sensitivity for the sensor, which can be related to the increase of the surface area. Through studies, using the DPV technique was possible to obtain a detection limit of 0.5 μM, a quantification limit of 1.8 μM, besides good results of repeatability. The sensor showed satisfactory recovery in the range of 98.1–103.3%, indicating that the method has good accuracy. The MnO<sub>x</sub>/MWCNT/GCE presented satisfactory behavior in the presence of similar molecules, with no significant interference, showing that the sensor proposed here can be an alternative in the determination of NaP in well water samples.

**Supplementary Information** The online version contains supplementary material available at <https://doi.org/10.1007/s44211-023-00374-w>.

**Acknowledgements** The authors are grateful to CAPES-PROCAD AM (Edital PROCAD AMAZÔNIA 2018—Line 2; Number SCBA: 88887.200615/2018-00), CNPq (PQ 2017, Proc. 310664/2017-9), FAPEMA (Proc. Edital UNIVERSAL-01136/17), ANP (Contract PMQC No. 1.028/2021; Research Project QUALIPETRO CON-SEPE-UFMA No. 2.460/22), and FAPESP (Grant 2018/12131-6 and 2017/22401-8) for the financial support and fellowships received, granted in the course of this research.

**Author contributions** ICBA conceptualization, methodology, investigation, writing—original draft. JRNS formal analysis, investigation. EPM resources, writing—review & editing. JKCS writing—review & editing. MAB formal analysis, data curation, writing—review & editing. NRS resources, writing—review & editing. ALBM conceptualization, Supervision Resources, Writing—review & editing.

**Data availability** Data will be made available upon request.

## Declarations

**Conflict of interest** There are no conflicts to declare.

## References

- V.A. Vasconcellos, V.F.C. Lins, R.A.D. Faria, *Int. J. Biosen. Bioelectron.* **5**, 142–1485 (2019). <https://doi.org/10.15406/ijb-sbe.2019.05.00168>
- Y. Pang, Y. Huang, W. Li, L. Feng, X. Shen, A.C.S. *Appl. Nano Mater.* **2**, 7785–7794 (2019). <https://doi.org/10.1021/acsnm.9b01821>
- Y.H. Pang, Y.Y. Huang, W.Y. Li, N.C. Yang, X.F. Shen, *Electroanalysis* **32**, 1459–1467 (2020). <https://doi.org/10.1002/ELAN.201900692>
- Q. Zhang, P. Liu, S. Li, X. Zhang, M. Chen, J. Liq. *Chromatogr. Relat. Technol.* **43**, 425–444 (2020). <https://doi.org/10.1080/10826076.2020.1746668>
- K. Sun, Y. Song, F. He, M. Jing, J. Tang, R. Liu, *Sci. Total Environ* **773**, 145403 (2021). <https://doi.org/10.1016/j.scitotenv.2021.145403>
- B. Kankanamge, K.K. Jinadasa, F. Monteau, S.W. Fowler, *Environ. Sci. Pollut. Res.* **27**, 20663–20674 (2020). <https://doi.org/10.1007/s11356-020-08305-2>
- I. Dosis, M. Ricci, H. Emteborg, H. Emons, *Anal. Bioanal. Chem.* **413**, 2283–2293 (2021). <https://doi.org/10.1007/s00216-021-03200-2/Published>
- Y. Meng, X. Liu, S. Lu, T. Zhang, B. Jin, Q. Wang, Z. Tang, Y. Liu, X. Guo, J. Zhou, B. Xi, *Sci. Total Environ.* **651**, 2497–2506 (2019). <https://doi.org/10.1016/j.scitotenv.2018.10.162>
- Ministério do meio ambiente, CONAMA, [http://conama.mma.gov.br/?option=com\\_sisconama&task=arquivo.download&id=676](http://conama.mma.gov.br/?option=com_sisconama&task=arquivo.download&id=676), accessed Jan 2023
- R. Preuss, J. Angerer, H. Drexler, *Int. Arch. Occup. Environ. Health* **76**, 556–576 (2003). <https://doi.org/10.1007/S00420-003-0458-1/FIG.S/1>
- C. Clark, T. Henderson, R. Royer, A. Brooks, R. McClellan, W. Marshall, T. Naman, *Fundam. Appl. Toxicol.* **2**, 38–43 (1982). [https://doi.org/10.1016/S0272-0590\(82\)80062-6](https://doi.org/10.1016/S0272-0590(82)80062-6)
- J.N. McDougal, D.L. Pollard, W. Weisman, C.M. Garrett, T.E. Miller, *Toxicol. Sci.* **55**, 247–255 (2000). <https://doi.org/10.1093/toxsci/55.2.247>
- R.D. White, *Drug Chem. Toxicol.* **22**, 143–153 (2008). <https://doi.org/10.3109/01480549909029728>
- J. Muñoz, C. Navarro-Senent, N. Crivillers, M. Mas-Torrent, *Microchim. Acta* **185**, 1–8 (2018). <https://doi.org/10.1007/s00604-018-2783-9>
- EUR-Lex - 32013L0039 - EN - EUR-Lex, (n.d.). <https://eur-lex.europa.eu/eli/dir/2013/39/oj> accessed 17 Jan 2023
- M. Zoveidavianpoor, *Recent insights in petroleum science and engineering* (SPi Global Croatia, 2018)
- K.K. Aswini, A.M. Vinu-Mohan, V.M. Biju, *Mater. Sci. Eng. C* **65**, 116–125 (2016). <https://doi.org/10.1016/J.MSEC.2016.03.098>
- J. Wang, Ü.A. Kirgöz, J.W. Mo, J. Lu, A.N. Kawde, A. Muck, *Electrochem. Commun.* **3**, 203–208 (2001). [https://doi.org/10.1016/S1388-2481\(01\)00142-4](https://doi.org/10.1016/S1388-2481(01)00142-4)
- M.A.T. Gilmartin, J.P. Hart, *Analyst* **120**, 1029–1045 (1995). <https://doi.org/10.1039/AN9952001029>
- B. Mekassa, M. Tessema, B.S. Chandravanshi, *Sens. Biosensing. Res.* **16**, 46–54 (2017). <https://doi.org/10.1016/J.SBSR.2017.11.002>
- H. Filik, A.A. Avan, *Arab. J. Chem.* **13**, 6092–6105 (2020). <https://doi.org/10.1016/J.ARABJC.2020.05.009>
- W. W. Anku, Ph. D. thesis, University of Johannesburg, South Africa (2017)
- Q. Guan, H. Guo, R. Xue, M. Wang, X. Zhao, T. Fan, W. Yang, M. Xu, W. Yang, *J. Electroanal. Chem.* **880**, 114932 (2021). <https://doi.org/10.1016/j.jelechem.2020.114932>
- X. Cao, X. Cai, N. Wang, *Sens. Actuat. B* **160**, 771–776 (2011). <https://doi.org/10.1016/j.snb.2011.08.061>
- S.A. Nsibandde, H. Montaseri, P.B.C. Forbes, *TrAC Trends Anal. Chem.* **115**, 52–69 (2019). <https://doi.org/10.1016/j.trac.2019.03.029>
- A. Azzouz, S. Kumar-Kailasa, S.S. Lee, A. Es, J. Rasc, E. Ballesteros, M. Zhang, K.-H. Kim, *TrAC Trends Anal. Chem.* **108**, 347–369 (2018). <https://doi.org/10.1016/j.trac.2018.08.009>
- A.L. Medina-Castillo, G. Mistlberger, J.F. Fernandez-Sanchez, A. Segura-Carretero, I. Klimant, A. Fernandez-Gutierrez, *Macromolecules* **43**, 55–61 (2010). <https://doi.org/10.1021/ma902095s>
- H. Li, F. Qu, *J. Mater. Chem.* **17**(33), 3536–3544 (2007). <https://doi.org/10.1039/b705743a>
- R.P. Toledo, C.E.S. Dias, D.R. Huanca, W.J. Salcedo, *Sens. Actuat. B* **277**, 445–455 (2018). <https://doi.org/10.1016/J.SNB.2018.09.043>
- A.S. Adeleye, J.R. Conway, K. Garner, Y. Huang, Y. Su, A.A. Keller, *Chem. Eng. J.* **286**, 640–662 (2016). <https://doi.org/10.1016/J.CEJ.2015.10.105>
- X. Ma, P. Huang, X. Dang, Y. Ai, D. Zheng, H. Chen, *Microchem. J.* **146**, 1026–1032 (2019). <https://doi.org/10.1016/J.MICROC.2019.02.031>
- P. Scherrer, *Kolloidchemie Ein Lehrbuch*, pp 387–409, (1912). [https://doi.org/10.1007/978-3-662-33915-2\\_7](https://doi.org/10.1007/978-3-662-33915-2_7)
- S. Boumaza, H. Kabir, I. Gharbi, A. Belhadi, M. Trari, *Int. J. Hydrogen Energy* **43**, 3424–3430 (2018). <https://doi.org/10.1016/j.ijhydene.2017.07.227>
- R.B.S. Sawczuk, H.A. Pinheiro, J.N. Ribamar-Santos, I.C.B. Alves, H.D.C. Viegas, C.A. Lacerda, J.C. Karla-Sousa, E.P. Marques, A.L.B. Marques, *Int. J. Environ. Anal. Chem.* (2021). <https://doi.org/10.1080/03067319.2021.1882446>
- M. Kölbach, S. Fiechter, R.V. Krol, P. Bogdanoff, *Catal. Today* **290**, 2–9 (2017). <https://doi.org/10.1016/j.cattod.2017.03.030>
- X. Luo, Q. Yang, Y. Dong, X. Huang, D. Kong, B. Wang, H. Liu, Z. Xiao, L. Zhi, *J. Mater. Chem. A* **8**, 17558–17567, (2022). <https://pubs.rsc.org/en/content/articlehtml/2020/ta/d0ta06238c>
- J.P. Barton, D.G. Infield, *IEEE Trans. Power Appar. Syst.* **19**, 441–448 (2004). <https://doi.org/10.1109/tec.2003.822305>
- C.C.L. McCrory, S. Jung, J.C. Peters, T.F. Jaramillo, *J. Am. Chem. Soc.* **135**, 16977–16987 (2013). <https://doi.org/10.1021/ja407115p>
- P. Connor, J. Schuch, B. Kaiser, W. Jaegermann, *Z. Phys. Chem.* **234**, 979–994 (2020). <https://doi.org/10.1515/zpch-2019-1514>
- D.T. Burns, K. Danzer, A. Townshend, *Pure Appl. Chem.* **74**, 2201–2205 (2003). <https://doi.org/10.1351/pac200274112201>
- W. Li, K. Diao, D. Qiu, Y. Zeng, K. Tang, Y. Zhu, Y. Sheng, Y. Wen, M. Li, *Food Chem.* **350**, 129229 (2021). <https://doi.org/10.1016/j.foodchem.2021.129229>
- J. Liang, L.-T. Bu, W.-G. Cao, T. Chen, Y.-C. Cao, *J. Taiwan Inst. Chem. Eng.* **65**, 584–590 (2016). <https://doi.org/10.1016/j.jtice.2016.06.005>
- N.T. Abdel-Ghani, G.A. El-Chaghaby, F.S. Helal, *J. Adv. Res.* **6**, 405–415 (2015). <https://doi.org/10.1016/J.JARE.2014.06.001>
- G. Yang, W. Yan, J. Wang, H. Yang, *CrystEngComm* **16**, 6907–6913 (2014). <https://doi.org/10.1039/C4CE00521J>
- Y. Wang, T. Hu, Y. Chen, H. Yuan, Y. Qiao, *Int. J. Hydrogen Energy* **45**, 22744–22751 (2020). <https://doi.org/10.1016/J.IJHYDENE.2020.06.085>
- C. P. Yi, S. R. Majid, *Semiconductors: growth and characterization*, edited by R. Iguanta, C. Sunseri, SPi Global, Croatia (2017). <https://doi.org/10.5772/INTECHOPEN.71957>
- J.C. Abrego-Martínez, Y. Wang, A. Moreno-Zuria, Q. Wei, F.M. Cuevas-Muñiz, L.G. Arriaga, S. Sun, M. Mohamedi, *Electrochim. Acta* **297**, 230–239 (2019). <https://doi.org/10.1016/j.electacta.2018.11.199>

48. R.A. Davoglio, G. Cabello, J.F. Marco, S.R. Biaggio, *Electrochim. Acta* **261**, 428–435 (2018). <https://doi.org/10.1016/j.electacta.2017.12.118>
49. F. Ataherian, K.T. Lee, N.L. Wu, *Electrochim. Acta* **55**, 7429–7435 (2010). <https://doi.org/10.1016/j.electacta.2010.01.102>
50. M. Dupont, A.F. Hollenkamp, S.W. Donne, *Electrochim. Acta* **104**, 140–147 (2013). <https://doi.org/10.1016/j.electacta.2013.04.007>
51. J. Jiang, A. Kucernak, *Electrochim. Acta* **47**, 2381–2386 (2002). [https://doi.org/10.1016/S0013-4686\(02\)00031-2](https://doi.org/10.1016/S0013-4686(02)00031-2)
52. R.V. McQuillan, G.W. Stevens, K.A. Mumford, *J. Hazard. Mater.* **383**, 121244 (2020). <https://doi.org/10.1016/J.JHAZMAT.2019.121244>
53. R.E. Sioda, B. Frankowska, Z.B. Lesiak, *Monatsh. Chem* **139**, 513–519 (2008). <https://doi.org/10.1007/s00706-007-0818-8>
54. R.E. Sioda, B. Frankowska, *J. Electroanal. Chem.* **568**, 365–370 (2004). <https://doi.org/10.1016/J.JELECHEM.2004.01.030>
55. G.A. Bhat, M. Periasamy, M.V. Bhatt, *Tetrahedron Lett.* **20**, 3097–3098 (1979). [https://doi.org/10.1016/S0040-4039\(01\)95329-8](https://doi.org/10.1016/S0040-4039(01)95329-8)
56. A.M. Santos, A. Wong, T.M. Prado, E.L. Fava, O. Fatibello-Filho, M.D.P.T. Sotomayor, F.C. Moraes, *Talanta* **224**, 121804 (2021). <https://doi.org/10.1016/j.talanta.2020.121804>
57. E.J.J. Laviron, *J. Electroanal. Chem. Interfacial Electrochem.* **101**, 19–28 (1979)
58. J.A. Bard, L.R. Faulkner, *Electrochemical Methods: Fundamentals and Applications* (John Wiley & Sons, Inc., New York, 2001)
59. M.M. Shanbhag, N.P. Shetti, S.J. Malode, R.S. Veerapur, K.R. Reddy, *FlatChem* **28**, 100255 (2021). <https://doi.org/10.1016/J.FLATC.2021.100255>
60. J. Mocak, A.M. Bond, S. Mitchell, G. Scollary, A.M. Bond, *Pure Appl. Chem.* **69**, 297–328 (1997). <https://doi.org/10.1351/pac199769020297>
61. H. Munawar, J.S. Mankar, M.D. Sharma, A. Garcia-Cruz, L.A.L. Fernandes, M. Peacock, R.J. Krupadam, *Talanta* **219**, 121273 (2020). <https://doi.org/10.1016/J.TALANTA.2020.121273>
62. X. Zhu, L. Lin, R. Wu, Y. Zhu, Y. Sheng, P. Nie, P. Liu, L. Xu, Y. Wen, *Biosens. Bioelectron.* **179**, 113062 (2021). <https://doi.org/10.1016/j.bios.2021.113062>
63. B. Sehatnia, R.E. Sabzi, F. Kheiri, A. Nikoo, *J. Appl. Electrochem.* **44**, 727–733 (2014). <https://doi.org/10.1007/s10800-014-0678-y>

Springer Nature or its licensor (e.g. a society or other partner) holds exclusive rights to this article under a publishing agreement with the author(s) or other rightsholder(s); author self-archiving of the accepted manuscript version of this article is solely governed by the terms of such publishing agreement and applicable law.